Transport Properties of Mixed-Matrix Membranes

A Kinetic Monte Carlo Study

Schneider, Daniel; Kapteijn, Freek; Valiullin, Rustem

Important note
To cite this publication, please use the final published version (if applicable).
Please check the document version above.

Transport Properties of Mixed-Matrix Membranes: A Kinetic Monte Carlo Study

Daniel Schneider,[1] Freek Kapteijn,[2] and Rustem Valiullin[1],[*]

[1]*Felix Bloch Institute for Solid State Physics, University of Leipzig, Linnéstr. 5, 04103 Leipzig, Germany*

[2]*Catalysis Engineering, Chemical Engineering Department, Delft University of Technology, van der Maasweg 9, 2629 HZ Delft, Netherlands*

Kinetic Monte Carlo (KMC) simulations are used to study transport of guest molecules in a two-phase medium in which the minority phase forms closed regions. This type of model system resembles compositions of mixed-matrix membranes (MMMs) made of a matrix and imbedded filler particles with different permeabilities. Based on an ideal filler-matrix composite morphology as defined in [H. Vinh-Thang, S. Kaliaguine, Chem. Rev. 113, 4980, 2013], the effects of the filler-particle volume fraction, particle size, shape (aspect ratio), and the spatial particle distribution on gas transport through MMMs are addressed. The results obtained for nonoverlapping and randomly placed spherical filler particles are found to be in good agreement with the analytical models available in the literature and have proven their good accuracy also for thin membranes where finite-size effects are expected to play an appreciable role. Furthermore, the prominent influence of the aspect ratio for nonspherical particles on the effective permeability is shown and scenarios are discussed where the alignment of the asymmetric filler particles give rise to anisotropic transport properties potentially favorable for the performance of MMMs. The KMC approach developed guides the optimal spatial arrangement and orientation of the filler particles for the different strategies to increase the membrane permeability and separation selectivity by transport enhancement or inhibition.

I. INTRODUCTION

Whilst the continuous development and facilitation of renewable clean-energy generation is required, fossil fuel remains a high-demanded energy source today and presumably in the next decades. With concerns about the anthropogenous climate change and its consequences on the rise, the reduction of greenhouse-gas emissions becomes vital. Most notably carbon dioxide and methane contribute to the human-caused greenhouse effect [1]. Thus, practicable CO_2 capture technologies can make a great difference [2]. Among those technologies, the application of membranes to separate carbon dioxide from the other emissions has considerable benefits over thermodynamically controlled gas-separation methods, being a continuous energy-efficient operation, having a small ecological and physical footprint, and a low complexity [3]. To this day, only polymeric membranes succeeded in large-scale industrial gas-separation realizations, mainly due to their low cost, simple processing, and mechanical stability [4]. However, as their most striking downside, they face an intrinsic limit in the trade-off between permeability and selectivity, the so-called Robeson upper bound [5,6]. Aside from that, the development of purely inorganic membranes consisting of materials including carbon

[7], zeolites [8], and metal-organic frameworks (MOFs) [9] attracted notable research interest. Among other advantages, those nanoporous materials feature a striking molecular selectivity, but suffer from other drawbacks such as low mechanical resistance and difficulties with large-scale manufacture.

A promising route to obtain the best of both worlds and to overcome mentioned limitations is to create composites, the so-called mixed-matrix membranes (MMMs), which consist of filler particles embedded in a polymer host matrix. MMMs have been shown to cross the Robeson upper bound limit of the polymeric membranes and at the same time providing solutions to the fabrication difficulties and low mechanical resistance of the inorganic materials [10,11]. Recently, MOF filler particles gained particular interest due to their high porosity and the ability to modify their chemical functionality by selecting appropriate building blocks or by postsynthetic treatment [12–14], thereby improving the compatibility between filler and matrix [15]. Considering MMMs, the shape of the filler particles also plays a prominent role for the membrane performance [16,17]. It is clear that the ability to produce MMMs tailor made for specific gas-separation applications requires a fundamental understanding of the transport properties of those composites.

Well-known theoretical approaches to study this cooperative transport behavior date back to the 1960s,

---

*valiullin@uni-leipzig.de

when the model previously developed by Maxwell [18] and generalized by Wiener for electrostatics was applied to investigate material permeability properties [19]. Over the years, other models and extensions to the Maxwell model have been presented by, amongst others, Lewis and Nielsen [20,21] and most recently in [22–24]. However, since the effective permeability of a composite membrane is not only determined by the permeabilities of the two components and their volume fraction, but additionally largely governed by the mixed-matrix-filler morphology [16,17], analytical models can only predict specific cases of simple polymer-filler geometries, and generally only *a posteriori* [24]. This highlights the convenience of a rigorous computational model, which can be applied to arbitrary composite morphologies such as the discrete lattice gas kinetic Monte Carlo (KMC) approach [25–28], which is used in this work to study the effects of filler-particle shape, size and distribution on the effective MMM permeability. In the advent of recent papers [29,30] questioning the applicability of the mentioned theoretical models to evaluate the performance of MMMs, by comparison with the computational results it is shown, for which cases the analytical predictions are valid and when they fail. Although important, eventual deviations from the ideal MMMs arising from fabrication or poor compatibility such as interfacial voids or rigidified polymeric regions at the polymer-filler interface [24] are not considered here due to the overwhelming complexity of the parameter space. Instead, the present work aims to give insight into the effective molecular transport properties of ideally compatible MMMs. This fundamental understanding enables the separation of the permeation behavior of the ideal membrane from the effects of the nonidealities and thus, also enables the study of the compatibility of filler and host in MMMs.

In the following, first a short revision of the Maxwell and Lewis-Nielsen models is given. Then the KMC approach applied to composite membranes is presented and verified with simple MMM morphologies featuring parallel and serially connected platelike domains (see also Appendix A). The effect of randomly distributed filler particles on the membrane permeability is evaluated and compared with theoretical predictions. Finally, the effective permeabilities of more complex geometries featuring filler particles of different size, shape and distribution are depicted and their consequences for the selectivity and membrane performance are presented.

II. METHODS

A. Analytical models

(a) The **Maxwell model**, originally developed for electrical conductivity of particulate composites, can be adapted to the relative effective permeability of

mixed-matrix membranes as follows [18]:

$$\frac{P_{\text{eff}}}{P_m} = \frac{2(1-\phi) + (1+2\phi)P_f/P_m}{(2+\phi) + (1-\phi)P_f/P_m}, \tag{1}$$

where ϕ denotes the volume fraction of the filler particles, P_f indicates the permeability of the considered gas species in the filler, and P_m is the permeability of the species in the pure polymer membrane. The Maxwell prediction disregards potential effects of filler-particle size, shape, and distribution. It is invalid in the region of high filler packing fractions ($\gg 0.2$), especially for large relative filler permeabilities P_f/P_m.

As an extension to the Maxwell model accounting for the effects of the filler-particle shape, a generalized Maxwell model can be expressed as [24]

$$\frac{P_{\text{eff}}}{P_m} = 1 + \frac{(1+G)\phi}{\frac{P_f/P_m+G}{P_f/P_m-1} - \phi}. \tag{2}$$

In Eq. (2), G is a heuristic geometric factor ranging from 0 for membranes built of serially connected plates to ∞ for parallel connected plates (both cases are addressed in Sec. III A). For $G = 2$, the original Maxwell equation for spherical filler particles [Eq. (1)] is retained.

(b) The **Lewis-Nielsen model** yields a more correct behavior for large filler packing fractions by factoring in the maximum packing fraction ϕ_{max}, e.g., $\phi_{\text{max}} = 0.64$ considering a random close packing of equal-sized spheres. The relative effective permeability can be predicted with [20,21]

$$\frac{P_{\text{eff}}}{P_m} = \frac{1 + 2\phi\frac{P_f/P_m-1}{P_f/P_m+2}}{1 - \phi\psi\frac{P_f/P_m-1}{P_f/P_m+2}}, \tag{3}$$

where

$$\psi = 1 + \frac{1-\phi_{\text{max}}}{\phi_{\text{max}}^2}\phi. \tag{4}$$

Note that for $\phi_{\text{max}} \to 1$, the Lewis-Nielsen model reduces to the Maxwell model [Eq. (1)].

B. Kinetic Monte Carlo simulations

In contrast to analytical predictions for the effective permeability of a gas species in MMMs, the on-lattice KMC method used in this work (modified from [31]) enables the simulation of arbitrary membrane-filler compositions. It also has advantages for addressing thin membranes in which finite-size effects may render analytical descriptions in the frame of effective-medium theories approximate. The Monte Carlo approach is chosen to estimate the solution of the diffusion equation because it is easy to implement and straightforward to apply to complex disordered
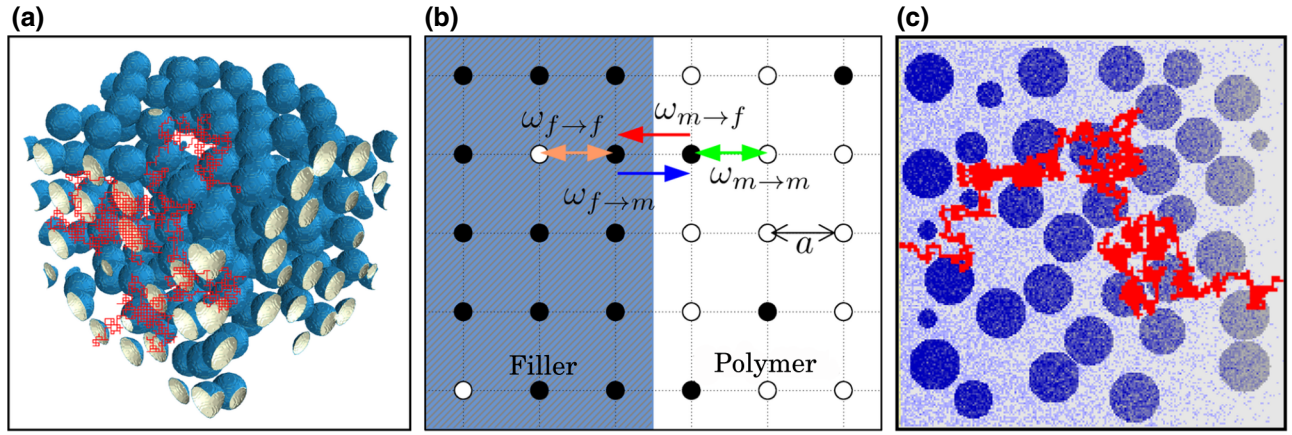
FIG. 1. Modeling and simulation scheme. (a) Three-dimensional representation of an example mixed-matrix membrane geometry featuring randomly placed nonoverlapping equal-sized spherical filler particles in blue and a possible molecular trajectory in red. (b) Magnified two-dimensional cut through the model exhibiting the underlying cubic lattice modeling the two subspaces and serving as a frame for the molecular movement. Arrows show the different jump probabilities in the subspaces and at the interface between them. (c) Two-dimensional cut through the geometry during a permeation simulation with the high-concentration environment (feed side) on the left and the low-concentration environment (permeate side) on the right. The different shades of blue show the concentration profile, in this specific case with high concentration in the filler particles. The red line indicates an example molecular trajectory.

morphologies. The following paragraphs are intended to give an extensive description of the KMC method used in this work.

In our simulations, the mixed-matrix morphology is represented in a coarse-grained way by a simple cubic lattice. Two mutually exclusive subspaces are considered, the polymer host membrane and the functional filler particles [see Fig. 1(a)]. Consequently, each node in the lattice representation either belongs to the polymer or the filler space [Fig. 1(b)]. The lattice spacing is determined by the discretization constant a. Additionally, the thus created grid serves as a discrete, coarse-grained frame for the molecular movements. In other words, a molecule can only reside in one node at a time and its motion is modeled by randomly chosen transitions to adjacent nodes at a certain transition (jump) rate. These transition rates are localized, i.e., regions in the mixed matrix with different transport properties also feature different rates. In the simulations, no explicit molecular interaction is considered. The hence obtained molecular trajectories are independent of each other, but are directly related to the mixed-matrix morphology. This resembles diffusive motion of a tracer molecule in a given environment and provides a statistical solution to the diffusion equation.

To model the different molecular transport rates in the subspaces representing polymer and filler, different local jump rates $r_{i \to j}$ are assigned to each bond between two adjacent nodes. In this way, the molecular trajectories become a function of the MMM geometry. By discretizing the time axis into time steps of length Δt, the local jump rates can be expressed as probabilities $\omega_{i \to j} = r_{i \to j} \Delta t$. Hence, to perform a jump, during a time step each

molecule rolls the dice twice, first to choose the direction (adjacent destination node or bond to travel through) and second to determine success or failure of the jump corresponding to the bond jump probability. If a jump attempt fails, the molecule remains in its current node. For the purpose of modeling MMMs with the two considered subspaces' polymer and filler, the definition of the following specific jump probabilities is sufficient: $\omega_{m \to m}$ for bonds with both current and destination nodes belonging to the polymer-host-membrane subspace; $\omega_{f \to f}$, if both nodes are in the filler-material subspace; and $\omega_{m \to f}$ ($\omega_{f \to m}$) if the current node is in the polymer, but the destination belongs to the filler (and vice versa). Additionally, to model the interface of the polymer membrane with the surroundings, the probabilities $\omega_{0 \to m}$ and $\omega_{m \to 0}$ are employed.

To give physical meaning to the transition probabilities, in the following they are related to physical properties such as molecular diffusivity, concentration, and permeability with the help of effective medium assumptions. The latter are similar to the assumptions needed to perform real permeation experiments. Using the subsequent relations, molecular transport through realistic materials can be simulated by adjustment of the jump probabilities.

(a) The *bulk diffusivities* of the subspaces can be adjusted via Einstein's law as follows:

$$D_m = \frac{\omega_{m \to m} a^2}{6 \Delta t}, \quad D_f = \frac{\omega_{f \to f} a^2}{6 \Delta t}. \tag{5}$$

Note that these diffusivities result only in an infinite isotropic medium.

(b) The *molecular concentrations* in the subspaces are determined by the equilibrium of the fluxes at the interfaces between (i) environment and MMM and (ii) polymer and filler. They are related to the bulk concentration c_0 via

$$c_m = \frac{\omega_{0 \to m}}{\omega_{m \to 0}} c_0, \quad c_f = \frac{\omega_{m \to f}}{\omega_{f \to m}} c_m. \tag{6}$$

(c) The *permeabilities* of the subspaces result from

$$P = DS = D\frac{c}{p_b}, \tag{7}$$

where S is the solubility or sorption equilibrium coefficient and p_b is the partial pressure of the species in the bulk gas phase. In Eq. (7), Henry's law is used for the second step. Note that Eq. (7) shows that the same effective MMM permeability can be obtained with different values for diffusivity D and concentration c. This means that the same effective macroscopic transport properties can be obtained with different underlying microscopic concentration profiles and molecular kinetics. In fact, Eq. (7) implies that the microscopic details of the molecular transport are irrelevant for the effective macroscopic quantities. Thus, for the sake of simplicity, only the subspace permeabilities P_m and P_f need to be considered. These considerations are verified by simulations using MMMs with varying diffusivities and concentrations in the two subspaces by keeping the subspace permeabilities constant. The results obtained in this way are identical for a given permeability irrespective of the diffusion and sorption properties (see Appendix B). For the message of this work only the relative permeability P_f/P_m is needed. To simulate specific values of P_f/P_m, the transition probabilities have to be chosen adequately to obey the following relation resulting from Eqs. (7), (5), and (6):

$$\frac{P_f}{P_m} = \frac{\omega_{f \to f}}{\omega_{m \to m}} \frac{\omega_{m \to f}}{\omega_{f \to m}}. \tag{8}$$

In order to emulate permeation experiments [Fig. 1(c)], an MMM film is brought into contact with a uniform high-concentration environment at one side (source) and a uniform low-concentration environment at the other side (sink). Due to the imposed concentration gradient, a net flux through the membrane from source to sink builds up. After a steady concentration profile within the membrane is attained, the net rate dN/dt of molecules passing through the membrane can be measured. This rate is related to the flux through the membrane as

$$J = \frac{1}{A}\frac{dN}{dt}, \tag{9}$$

where A denotes the membrane area in the plane perpendicular to the direction of the concentration gradient. Via Fick's first law, the molecular flux can be related to the diffusion and the permeability coefficient as follows:

$$J = -D\frac{dc}{dx} = -P\frac{dp}{dx} = P\frac{p_0 - p_1}{z}, \tag{10}$$

where z indicates the membrane thickness and p_0 and p_1 the partial pressure of the gas species at source and sink, respectively. To obtain the effective permeability of the MMM relative to the permeability of the pure polymer membrane, the following relation originating from Eqs. (9) and (10) can be used:

$$\frac{P_{\text{eff}}}{P_m} = \frac{J_{\text{eff}}}{J_m} = \frac{dN_{\text{eff}}}{dN_m}. \tag{11}$$

Another convenient advantage of the effective medium theories is that it is possible to correlate the jump probabilities in the KMC approach [Eq. (8)] to realistic filler and host permeabilities obtained from permeation experiments with the pure bulk materials. For this purpose, at selected thermodynamic conditions and with one or more gas species of choice, the permeabilities in both a pure polymer membrane and a pure filler material may be measured independently and passed on to the presented KMC approach. The simulations are then able to predict the effective permeabilities of the chosen gases in a MMM combined of the two materials with any arbitrarily chosen filler-host composition.

This approach remains valid as long as those material permeabilities are intensive properties, i.e., transport limitations due to surface effects are low. However, in the case of existing significant surface barriers for either host or filler material, the approach can still be used under the constraint that the permeation experiments with the pure materials have to be done with a film thickness d_{exp} adjusted according to the average size of the domains in the considered MMM. Thus, for the host membrane, this means $d_{\text{exp,host}} = d_{m,\text{MMM}}$ and for the filler that $d_{\text{exp,filler}}$ is equal to the average size of the filler particles in the MMM in the direction of flow. Note that the effects of adsorption saturation and competitive adsorption are intrinsically included in the permeability parameters taken from the experiments and do not need to be modeled specifically. This is again a consequence of the effective medium assumption, which has to be presumed for the permeation measurements as well. Note that this means that instead of relying on a mechanistic transport model predicting membrane performance based on applied operation conditions, the presented KMC method uses an effective medium approach incorporating all molecular mechanisms in the fixed effective subspace permeabilities. The methodology of using measured material permeabilities in our KMC simulations was proven for a specific MMM in Ref. [32]. The present work, however, is focused on giving a general understanding of the molecular transport in

ideally compatible MMMs. Hence, in the following we study MMMs over material permeability ranges instead of considering specific polymer and filler permeabilities, P_m and P_f, from experiments.

III. RESULTS AND DISCUSSION

To be able to improve the separation performance of MMMs, it is crucial to establish how the integration of the filler material into the membrane affects the mass transport of the guest molecules. This section demonstrates the effects of filler particles of different packing density, size, shape, and distribution type on the transport properties in ideal MMMs, i.e., in MMMs in which no additional transport resistances or void layers are formed at the interfaces between the polymer and filler phases (so-called MMMs of ideal morphology [24]). First, the limiting scenarios of parallel and serially connected plates of polymer and filler material are presented.

The following two cases are defined to simplify further reference.

(a) *Transport enhancement* ($\mathcal{P}_+$): Inclusion of filler material into the membrane exhibiting a higher permeability regarding the considered gas species than the pure membrane, $P_f > P_m$, is expected to lead to an increase of the effective mixed-matrix-membrane permeability P_{eff}.

(b) *Transport inhibition* ($\mathcal{P}_-$): Inclusion of filler material into the membrane of lower permeability with respect to the gas species in consideration than the pure membrane, $P_f < P_m$, is predicted to decrease the effective mixed-matrix-membrane permeability P_{eff}.

Additionally, in the following the direction parallel to the flow through the membrane is refered to by the abbreviation $\|_{\text{flow}}$, while the perpendicular directions are labeled $\perp_{\text{flow}}$.

A. Limiting cases: parallel and serially connected plates

In order to obtain a general understanding of the transport properties in MMMs, the two cases of layered membranes $\|_{\text{flow}}$ and $\perp_{\text{flow}}$ are studied (for a graphical representation see the insets in Figs. 2 and 3). Regarding the tortuosity of the subspaces,

$$T = \frac{L}{C}, \tag{12}$$

i.e., the length of a curve, L, relative to the linear distance C between its ends, these two cases represent extreme scenarios. The first case of layers of polymer and filler material aligned $\|_{\text{flow}}$ exhibits the lowest possible tortuosity, $T = 1$. On the other hand, the layers arranged $\perp_{\text{flow}}$ feature maximum tortuosity, $T \to \infty$. In consequence, for
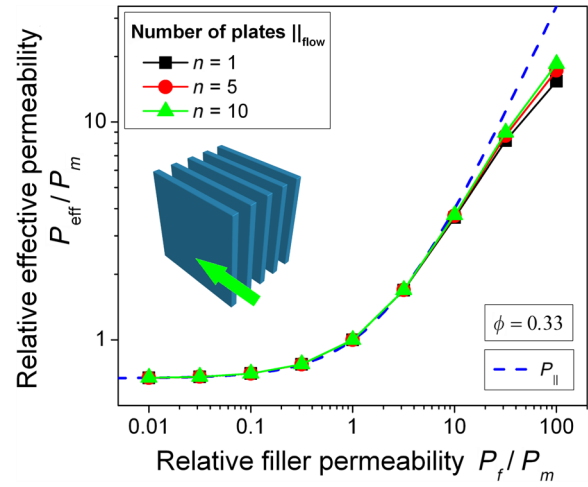

FIG. 2. Effective permeability versus filler permeability relative to the permeability of the pure polymer, P_m, for mixed-matrix membranes featuring a filler subspace divided into one (*black squares*), five (*red circles*), and ten (*green triangles*) plates aligned $\|_{\text{flow}}$. The dashed blue line denotes the prediction from the parallel circuit analog [Eq. (13)]. The mixed-matrix composition with five plates is shown in the inset. The green arrow denotes the direction of flow. All three geometries have a filler volume fraction of 0.33.

the permeation through MMMs, these two cases encompass the region of possible effective permeability values independent of the composition of the two subspaces, as shown in the following.
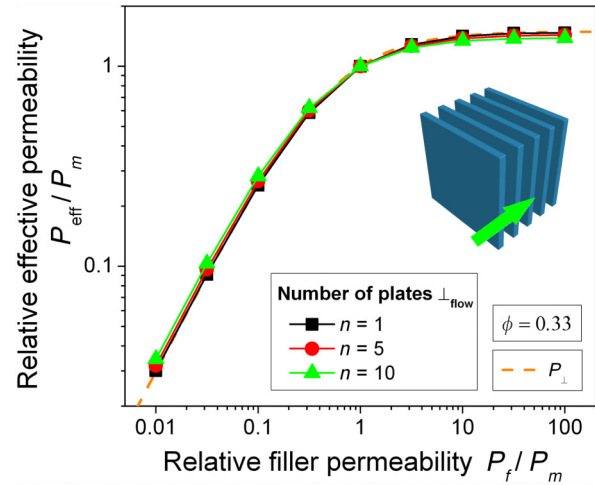

FIG. 3. Effective permeability versus filler permeability relative to the permeability of the pure polymer, P_m, for mixed-matrix membranes featuring a filler subspace divided into one (*black squares*), five (*red circles*), and ten (*green triangles*) plates aligned $\perp_{\text{flow}}$. The *dashed orange* line denotes the prediction of the series circuit analog [Eq. (15)]. The mixed-matrix composition with five plates is shown in the inset. The green arrow denotes the direction of flow. All three geometries have a filler volume fraction of 0.33.

1. Plates $\parallel_{flow}$

Similar to the conductance in parallel electrical circuits [18], the effective permeability of a membrane featuring plates aligned $\parallel_{flow}$ can be predicted by the weighted average

$$P_\parallel = a_m P_m + a_f P_f, \tag{13}$$

where a_k denotes the volume fraction of subspace $k \in \{m, f\}$ or, similar for the considered composition, the relative effective area of the subspace $\perp_{flow}$ ($a_m + a_f = 1$). Equation (13) is identical to the generalized Maxwell model [Eq. (2)] with $G = \infty$. The comparison of Eq. (13) with the simulation results in Fig. 2 validates this prediction. Regardless of into how many plates the subspaces are divided, there is a good agreement with the analytical expression. For very low filler permeabilities, the contribution of the filler subspace vanishes, since the filler material is nearly impermeable for the gas molecules and thus, $P_{\text{eff}}/P_m \rightarrow a_m$. For high filler permeabilities, only the filler material significantly contributes to the permeability and thus, $P_{\text{eff}}/P_m \rightarrow a_f P_f/P_m$. The deviations between the analytical prediction and the computational results in this regime are due to artifacts of the discrete model for the molecular motion at the surfaces between the domains and vanish for lattice constants $a \rightarrow 0$ and for $T \gg 1$ (see, e.g., the very good agreement with the Maxwell model for spherical filler particles in Fig. 4). The considered mixed-matrix composition is continuous $\parallel_{flow}$ ($T \rightarrow 1$) and thus, imposes no diffusive limitations due to tortuosity on the guest molecules in this direction. Consequently, Eq. (13) indicates the upper boundary for the effective permeability, independent of the underlying polymer-filler composition. Additionally to the effective permeability, the average total dwell times of the molecules in the two subspaces τ_m and τ_f, and the total dwell time $\tau_\parallel$ in the membrane are related as

$$\frac{1}{\tau_\parallel} = \frac{a_m}{\tau_m} + \frac{a_f}{\tau_f}, \tag{14}$$

resembling the resistance in electrical circuits.

2. Plates $\perp_{flow}$

The case of filler plates aligned $\perp_{flow}$ can be treated analogous to serially connected electrical circuits. Hence, similarly to the electrical conductance [18], the effective permeability can be expressed as

$$\frac{1}{P_\perp} = \frac{l_m}{P_m} + \frac{l_f}{P_f}, \tag{15}$$

where l_k indicates the volume fraction of subspace $k \in \{m, f\}$ or synonymously for the composition in consideration, its total relative length in the direction $\parallel_{flow}$ ($l_m + l_f$
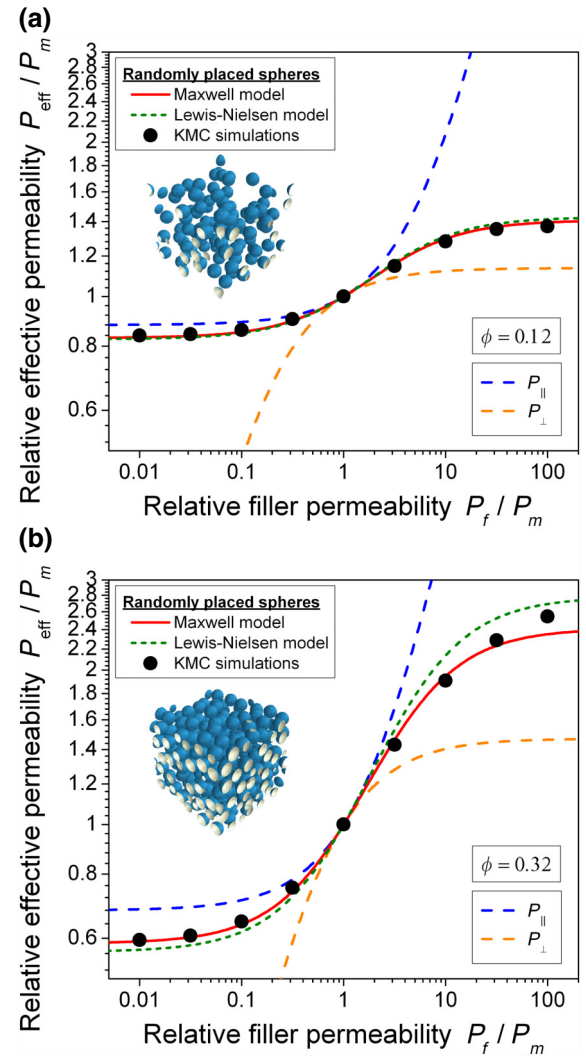

(a)

(b)

FIG. 4. Effective permeability versus filler permeability relative to the permeability of the pure polymer, P_m, for mixed-matrix membranes featuring randomly placed nonoverlapping spherical particles as shown in the insets. The packing fractions are 0.12 (a) and 0.32 (b) and the particle radius is chosen to be 1/15 of the membrane thickness. The black dots indicate the results of the KMC simulations, the solid red line depicts the Maxwell model [Eq. (1)], and the dotted green line represents the Lewis-Nielsen prediction [Eq. (3)]. The *dashed blue* and the *dashed orange* lines are based on Eqs. (13) and (15), respectively. They encompass the region of possible effective permeabilities.

$= 1$). Equation (15) is identical to the generalized Maxwell model [Eq. (2)] with $G = 0$. The validity of Eq. (15) is shown by its coincidence with the simulation results in Fig. 3. Independent of the number of plates the subspaces are divided in (i.e., independent of the filler domain size $\parallel_{flow}$), for filler permeabilities $P_f \ll P_m$, the relative effective permeability approaches $P_f/(l_f P_m)$, while large filler permeabilities lead to $P_{\text{eff}}/P_m \rightarrow 1/l_m$. Since the polymer-filler composition exhibits maximum tortuosity,

the diffusion-limiting subspace is always the slower one, with the fast subspace having only small local influence. Consequently, for the permeation through mixed-matrix membranes, Eq. (15) indicates the lower boundary for the effective permeability, independently of the composition of the two subspaces. The average dwell times of the molecules are related similarly to the electric resistance in a series circuit as

$$\tau_\perp = l_m \tau_m + l_f \tau_f. \tag{16}$$

B. Transport modification by filler particles

Considering arbitrary guest species, by incorporating a filler material of permeability $P_f \neq P_m$ into the polymer host membrane, the effective permeability of the membrane, P_{eff}, is subject to change yet alone by local mass transfer modifications due to the transport behavior of the gas in the filler material itself, regardless of the spatial composition of the mixed matrix. This potential for the change in effective permeability is described by Eq. (13), which, as shown earlier, is accurate for polymer-filler compositions as long as autocorrelations in the molecular trajectories stay insignificant (membrane tortuosity $T \to 1$ or $P_f/P_m \to 1$). With ϕ denoting the total volume fraction of the filler particles, Eq. (13) with $a_f = \phi$ and $a_m = 1 - \phi$ is represented by the dashed blue lines in Fig. 4. The black dots indicate the effective permeabilities obtained from the kinetic Monte Carlo simulations for MMMs with randomly placed nonoverlapping spherical filler particles. The discrepancy between the upper boundary for the maximum achievable effective permeability as given by Eq. (13) and the simulation results is attributed solely to the spatial composition of the filler material affecting the tortuosity of the molecular trajectories during their transit through the membrane. To verify the computational approach, the Maxwell model prediction [Eq. (1)] is shown in red. It nicely coincides with the data obtained from the simulations, even up to a packing fraction of 0.32, except for high filler permeabilities, where the Maxwell model becomes less accurate. In this region, the results obtained from the simulations approach the Lewis-Nielsen model [Eq. (3)], shown with the dotted green line. In general, the results reveal that for $P_f < P_m$, the effective permeability of the membrane is decreased, indicating transport inhibition ($\mathcal{P}_-$). This is due to the filler particles being high-resistance obstacles for the passing gas molecules. Firstly, these obstacles slow down molecules migrating through them. Secondly, they increase the probability for long, more tortuous molecular trajectories avoiding them. However, since there is still a high probability for continuous pathways not severely affected by the obstacles, the ideal inhibiton potential of Eq. (15) with $l_f = \phi$ and $l_m = 1 - \phi$ (dashed orange line) cannot be reached. For nearly impermeable filler particles ($P_f \ll P_m$), the curve reaches a plateau. On the other hand, for $P_f > P_m$, the permeability of the mixed-matrix membrane is enhanced, indicating the $\mathcal{P}_+$ case. The curve is nearly linear for $P_f \gtrsim P_m$, but becomes saturated for very large P_f. In this regime, the filler particles act as fast transport pathways accelerating the guest molecules in their realm. However, the simulation results show that the potential of enhancement predicted by Eq. (13) can barely be attained, since the probability of the randomly moving molecules to find a fast continuous pathway of filler particles through the membrane remains low. For detailed description of this phenomenon and of particular details determining transport enhancement under these conditions see Refs. [28,33]. By comparison of the top and bottom graph in Fig. 4, it can be seen that elevated filler packing fractions amplify the inhibiting ($\mathcal{P}_-$) or intensifying ($\mathcal{P}_+$) effects on transport. This amplification for higher ϕ is based on both increased effects on local transport (dashed blue lines) and tortuosity effects, i.e., molecules have to overcome more high-resistance obstacles while $\mathcal{P}_-$ or there is a higher probability for fast transport pathways when $\mathcal{P}_+$.

C. Effects of particle size

To study the effects of filler-particle size on the effective permeability of MMMs, four different polymer-filler compositions exhibiting randomly distributed spherical particles of different size, but with the same total volume fraction of the filler subspace are created (see Fig. 5). However, Fig. 6 shows only marginal deviations between
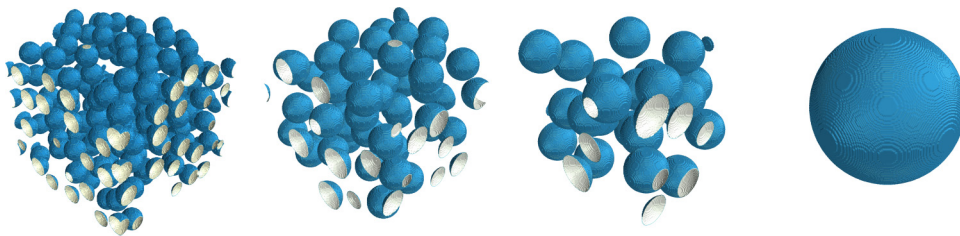

FIG. 5.   Mixed-matrix membrane geometries of randomly placed nonoverlapping spherical filler particles of different diameter; *from left to right*: 0.133, 0.2, 0.267, and 0.752 in units of the membrane diameter. The packing volume fraction is chosen to be 0.22 and is equal in all four geometries.
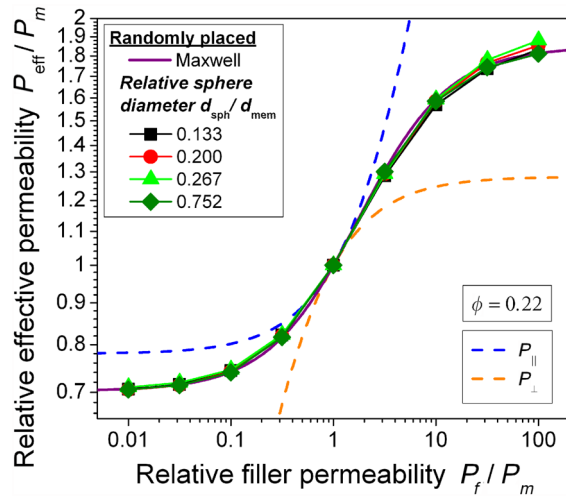
FIG. 6. Effective permeability versus filler permeability relative to the permeability of the pure polymer, P_m, for the mixed-matrix membranes shown in Fig. 5. The sphere diameters relative to the membrane thickness are 0.133 (*black squares*), 0.2 (*red circles*), 0.267 (*green triangles*), and 0.752 (*dark-green diamonds*). The *dashed blue* and *dashed orange* line encompass the possible effective permeabilities region based on Eqs. (13) and (15), respectively.

the compositions in consideration, proving the effective permeability to be largely independent of the filler-particle size for ideal MMMs. Remarkably, from these results obtained for the low packing fraction 0.22, it can be inferred that the Maxwell model [Eq. (1)] delivers the correct prediction for randomly placed spherical particles regardless of their size.

D. Random versus regular distribution

Figure 7 shows the relative effective permeability upon variation of the permeability of the filler material for mixed-matrix morphologies with randomly and regularly

distributed spherical filler particles. The red squares indicate the results for the mixed-matrix geometry featured in the top right of Fig. 7 for a particle diameter of 0.133 in units of the membrane thickness. However, as found in the previous section, the red squares are representative for every particle size for at least not too large filler packing fractions, even for the extreme case, where all the filler subspace is combined into one large particle. In this case, random and regular distributions have the same morphology, i.e., the same effective permeability. By decreasing the particle size for the regular distribution (*green diamonds* and *black dots*), the MMM permeability is in principle unaffected. Also shown in Fig. 7 is the Maxwell prediction, revealing that for nonoverlapping filler particles and reasonably low packing volume fractions (here $\phi = 0.27$) it is valid for both the random and regular distribution.

The similar results for the regular lattice arrangements of different particle sizes support the notion of the permeability as material property. The geometry with the regularly arranged particles can be divided into similar unit cells of equal morphology. Then the permeability of one unit cell should be equal to the permeability of any other unit cell and similarly, equal to the permeability of the whole membrane. This is valid as long as the correlation length of the molecular trajectories affected by the MMM morphology is small compared to the membrane size. In other words, as long as the molecular transport in the membrane is effectively homogeneous. This effective medium behavior also explains the similar results for randomly distributed particles of different sizes in the previous section (Fig. 6). Here, although no unit cell exists, a sufficiently large arbitrarily chosen subsection of the membrane should have similar permeability to any other sufficiently large subsection or to the membrane as a whole. For MMMs with heterogeneous transport, the effective medium approach breaks. Such morphologies include (for many, but not all conditions) membranes with only very few randomly distributed filler particles or membranes with many filler particles and
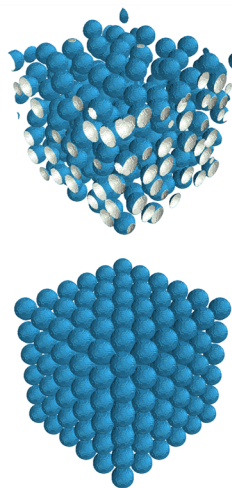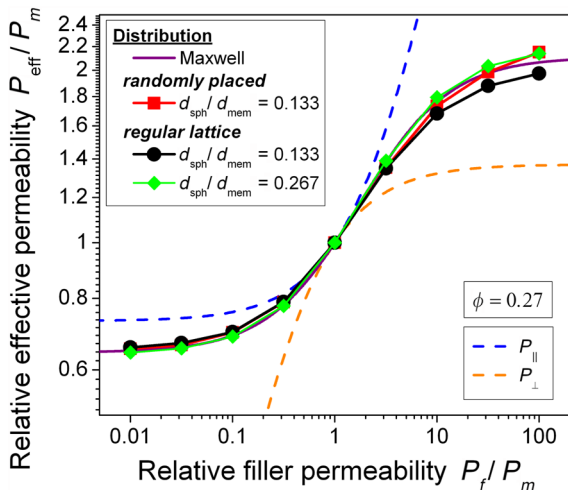

FIG. 7. Effective permeability versus filler permeability relative to the permeability of the pure polymer, P_m, for mixed-matrix membranes with different types of filler-particle distributions. The *red squares* indicate randomly placed spheres (as shown in the top right) while the *black circles* and the *green diamonds* represent a regular cubic lattice composition (shown in the bottom right). The *dashed blue* and the *dashed orange* line emcompass the region of possible effective permeabilities based on Eqs. (13) and (15), respectively. In all geometries the filler packing fraction is chosen to be 0.27 and the particle diameter in units of the membrane thickness is shown in the inset.
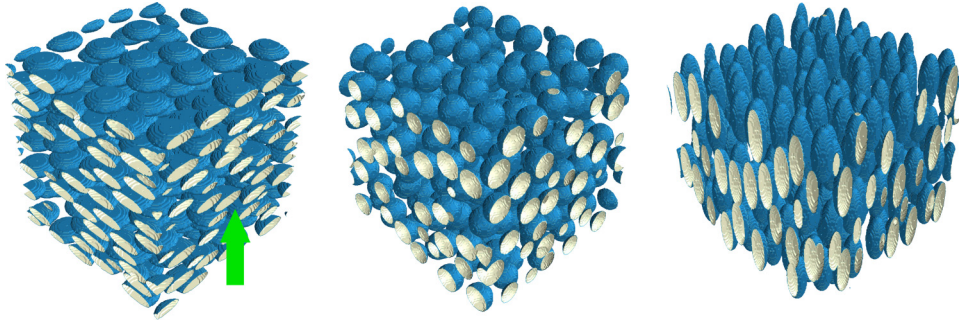
FIG. 8. Mixed-matrix membrane geometries of randomly placed nonoverlapping filler particles of different aspect ratios: disk-shaped (*left*), spherical (*center*), and rodlike (*right*). The particle volume is kept constant under change of shape. The concentration gradient during the permeation simulations is applied to the vertical direction in the paper plane as indicated by the green arrow. The packing fraction is chosen to be 0.32 and the particle radius is 1/15 of the membrane diameter.

high loading, where the particles merge into random larger structures. When changes in permeability are observed with variations in filler-particle size, it may also be a strong indicator for strong surface effects between host membrane and filler particles. Then, the effective permeability of the membrane is subject to the different surface to volume ratios and the changing correlations in the molecular trajectories originating from the surface effects.

E. Effects of particle shape

To unveil the effects of the particle shape on molecular transport, membrane models with randomly placed nonoverlapping ellipsoidal particles with different aspect ratio between the directions $\|_{\text{flow}}$ and $\perp_{\text{flow}}$, but similar volumes are studied (see Fig. 8). As Fig. 9(a) shows, throughout the entire filler permeability range, the rodlike-shaped particles deliver the highest effective permeability, leading to the least transport inhibition of the three shapes for $\mathcal{P}_-$, but the largest enhancement for $\mathcal{P}_+$. In contrast, the disk-shaped particles always deliver the lowest P_{eff}, exhibiting the most pronounced transport inhibition for $\mathcal{P}_-$, but the least significant enhancement at $\mathcal{P}_+$. The left side of Fig. 9(a) also features curves obtained with the generalized Maxwell model [Eq. (2)] for different geometric fractors G, showing very good correspondence of the simulation
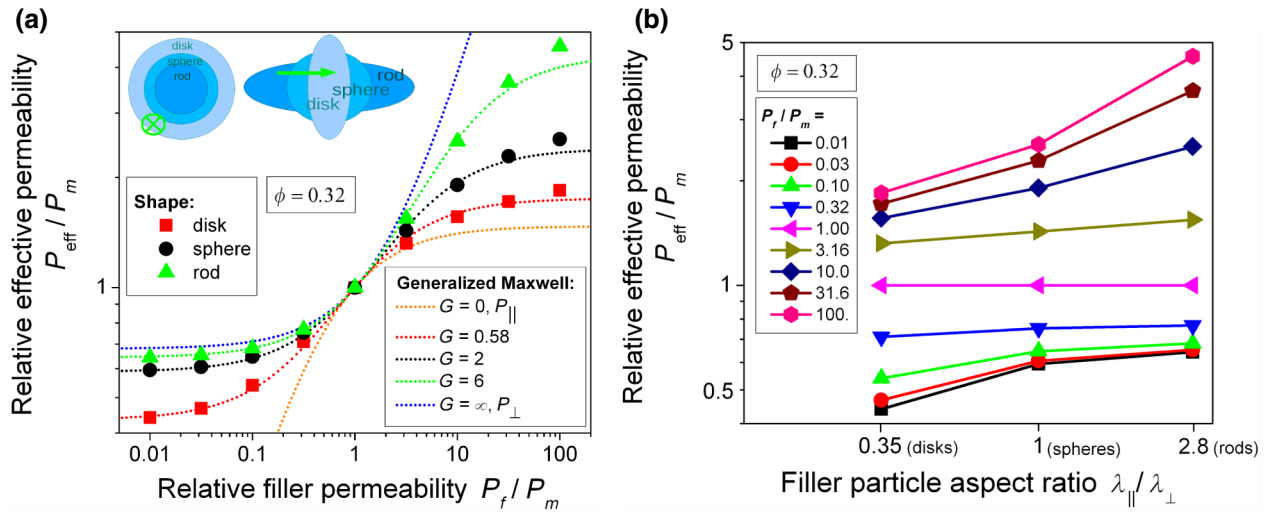

FIG. 9. (a) Effective permeability versus filler permeability relative to the permeability of the pure polymer, P_m, for the mixed-matrix membranes featuring randomly placed particles of different shapes with a filler packing fraction of 0.32 as shown in Fig. 8. The *red squares* indicate disk-shaped filler particles, the *black circles* spherical particles, and the *green triangles* rodlike particles as obtained from the kinetic Monte Carlo simulations. The *dotted* lines show the generalized Maxwell model [Eq. (2)] with different values for the geometric factor G, where the two extreme cases indicated by the *dotted blue* and the *dotted orange* line emcompass the region of possible effective permeabilities. For comparison, all three particle shapes are shown in the inset. The direction of flow is indicated by the green arrows. (b) Relative effective permeability versus filler-particle aspect ratio $\|_{\text{flux}}$. Different relative filler permeabilities are shown as specified in the legend. As shown with the x-axis labels, the aspect ratios correspond to the geometries with disk-shaped, spherical, and rodlike filler particles.

results with the predictions, except, as shown earlier in Fig. 4, in the region of very high filler permeabilities, where the Maxwell model is inaccurate. The G factors related to the disk-shaped and rodlike particles where chosen by least-squares best fit. For comparison purposes, Fig. 9(a) additionally features the upper and lower boundary of the effective permeability with the dashed blue and orange lines, Eqs. (13) and (15), respectively. The permeability of the geometry exhibiting the rods occurs to approach most the upper boundary curve, indicating the least significant influence of the transport resistance due to the spatial filler composition in the direction $\parallel_{\text{flow}}$, i.e., the lowest tortuosity, while the geometry featuring the disks shows the largest compositional transport suppression, i.e., the highest tortuosity. In other words, for the $\mathcal{P}_-$ case, the disklike filler particles are most efficient in modulating the effective permeability, while for the $\mathcal{P}_+$ case, the rodlike particles are the best choice out of the three. Figure 9(b) shows the relationship between the filler-particle aspect ratio $\lambda_\parallel/\lambda_\perp$ and the modification of the effective permeability of the mixed-matrix membrane in more detail. The slopes of the curves for low ($\mathcal{P}_-$) and elevated ($\mathcal{P}_+$) filler permeabilities indicate the influence of the shape on mass transfer. In the P_+ case, an increase in the particle dimensions $\parallel_{\text{flow}}$ leads to a rise in effective permeability. This is due to on average more continuous fast transport pathways through the membrane for this aspect ratio. Being only marginal for $P_f \gtrsim P_m$, this effect intensifies for very high filler permeabilities. Similarly, for the $\mathcal{P}_-$ case the effective permeability drops with decreasing aspect ratio $\parallel_{\text{flow}}$, especially for very low P_f.

F. Selectivities and MMM performance

In this section, the relationship between the mixed-matrix composition on the one side and the membrane selectivity and performance on the other side is studied. In particular, the mixed-matrix compositions shown in Fig. 8 featuring randomly placed filler particles of different shape are considered. To simplify the studies, in the following, the fitting function for the relative effective permeability

$$P_r \equiv \frac{P_{\text{eff}}}{P_m} = 1 - \frac{\phi\left(1 - P_f/P_m\right)}{\lambda_\parallel\left(1 - P_f/P_m\right) + P_f/P_m} \quad (17)$$

is used to obtain heuristic analytical expressions for the relative effective permeabilities of the corresponding membrane geometries. Equation (17) is obtained for intermediate compositions between the two extreme cases of plates aligned $\parallel_{\text{flow}}$ and $\perp_{\text{flow}}$ as shown in Appendix C. Note that with the help of Eq. (17), P_{eff} can be related to an average measure of the filler domain size $\parallel_{\text{flow}}$, $\lambda_\parallel$, which is also the fitting parameter adjusted to approximate the permeability data from the KMC simulations. It turns out that Eq. (17) is an alternative expression for the generalized Maxwell

model [Eq. (2)] with $\lambda_\parallel = (\phi + G)/(1 + G)$. Utilizing Eq. (17), the relative selectivity α_r between two gas species, fast ("permeate") and slow ("retentate"), can be studied readily for a given mixed-matrix composition with

$$\alpha_r = \frac{P_{r,\text{fast}}}{P_{r,\text{slow}}}. \quad (18)$$

This is presented for a wide range of fast and slow species permeabilities in the polymer and filler subspaces in Fig. 10 for the mixed-matrix geometries with randomly placed disk-shaped and rodlike particles. For specific applications, the relative selectivities can be converted to absolute values using

$$\alpha = \alpha_r \frac{P_{m,\text{fast}}}{P_{m,\text{slow}}}, \quad (19)$$

where $P_{m,\text{fast}}$ and $P_{m,\text{slow}}$ denote the permeabilities of fast and slow species in the pure polymer host material, respectively, obtained from experimental studies. Figure 11 shows for which fast-slow pairs the rodlike or the disk-shaped particles yield the larger selectivity. In a more general sense, it elucidates when it is favorable for the selectivity to align the long sides of arbitrarily shaped filler particles $\parallel_{\text{flow}}$ or $\perp_{\text{flow}}$.

As shown in the Robeson plot [5,6], an increase in separation performance can be achieved through an improved selectivity on the one hand and through an elevated permeability of the fast gas species on the other hand. To achieve a more comprehensive measure of the performance of a MMM, both the selectivity and the relative effective permeability of the fast species may be combined into one membrane improvement factor, e.g.,

$$f_r = \alpha_r^k P_{r,\text{fast}}^l, \quad (20)$$

with the two characteristic properties weighted according to the specific needs of the individual application with the help of the exponents k and l. This approach is borrowed from mathematical optimization. Given a specific fast-slow pair, the aim is to find the mixed-matrix materials and morphology yielding the maximum improvement factor. By using the permeabilities in the pure polymer obtained from permeation experiments, an absolute measure of membrane performance may be obtained as follows:

$$f = f_r \frac{P_{m,\text{fast}}^{k+l}}{P_{m,\text{slow}}^k}. \quad (21)$$

For simplicity, here it is chosen to give the selectivity and the permeability of the fast-species equal weight, i.e., $k = l = 1$. In reality, the choice of k and l is governed by efficiency aspects of the application, i.e., to which extent a higher selectivity or a higher flux is technologically and
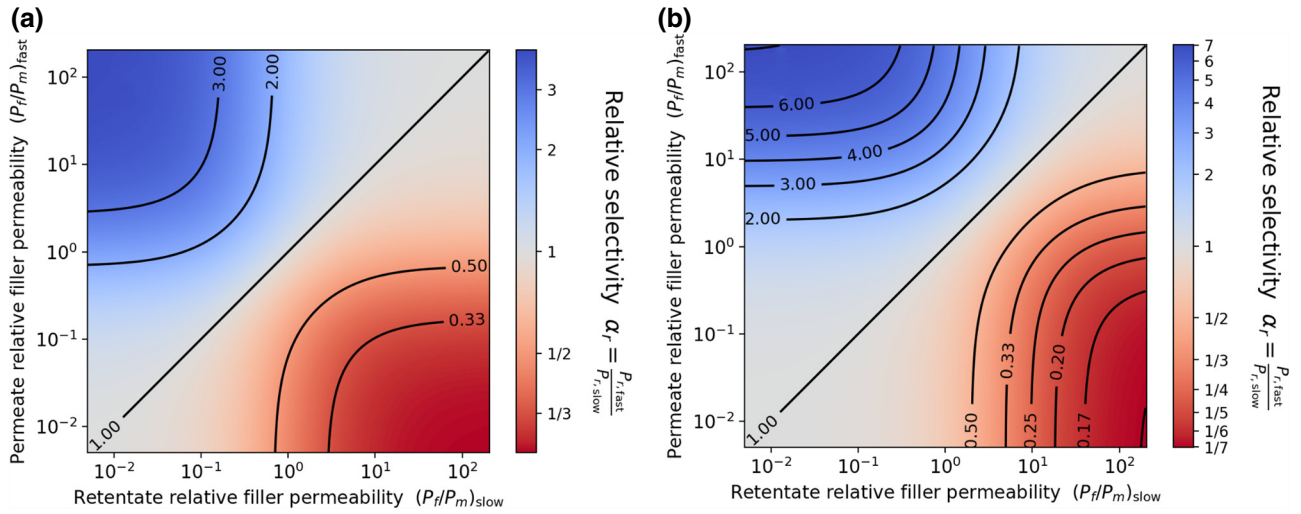
FIG. 10.   Colormaps showing the relative selectivities between fast ("permeate") and slow ("retentate") species for a wide range of relative filler permeabilities for the mixed-matrix compositions with randomly distributed disk-shaped (a) and rodlike (b) filler particles featured in Fig. 8 ($\phi = 0.32$). Blue regions are favorable as they indicate an increase in selectivity due to the filler particles, while red regions exhibit a selectivity decrease. The relative values can be converted into absolute selectivities with the help of Eq. (19).

economically more desired. Figure 12 shows the improvement factor for a wide range of fast- and slow-species subspace permeabilities in the membrane geometries featuring randomly placed disk-shaped and rodlike particles. Finally, Fig. 13 presents the ratio of the improvement factors of MMMs with rodlike and disk-shaped filler particles, giving insight about for which fast-slow pairs the long sides of the filler particles better be aligned $\parallel_{\text{flow}}$ or $\perp_{\text{flow}}$ for maximum membrane improvement. The geometry of
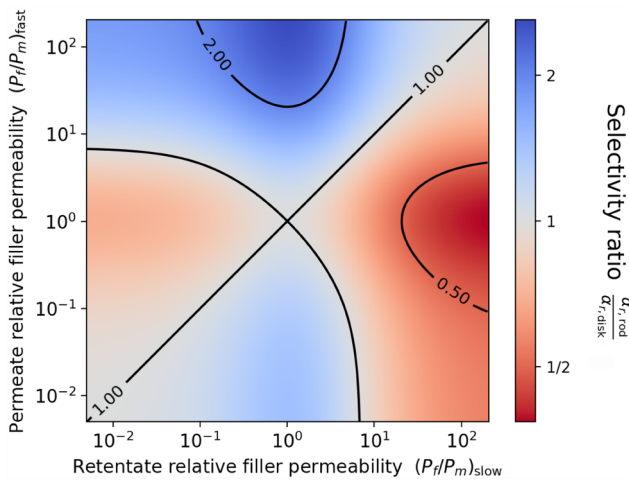

FIG. 11.   Colormap obtained by setting the selectivities of the mixed-matrix compositions featuring rodlike and disk-shaped filler particles in relation to each other ($\alpha_{r,\text{rod}}/\alpha_{r,\text{disk}}$). The blue regions in the (fast, slow)-species-relative filler permeability space indicate higher selectivities for the rodlike over the disk-shaped particles. In the red regions, the disk-shaped particles yield more favorable selectivities.

choice for most of the fast-slow pairs features particles with their long sides aligned $\parallel_{\text{flow}}$. This result is somewhat counterintuitive as often disk-shaped filler particles are striven for, although it should be noted that the maximum aspect ratio investigated ranged only from 1/3 to 3. More generally, it is concluded that disk-shaped geometries are preferred for regions where the permeability of the fast component in the filler is of the same order as in the polymer, as observed for CO_2/CH_4 separation [17], while the rod-shaped filler particles are preferred for regions where the permeability of the slow component in the filler and the polymer are of the same order.

IV. DISCUSSION

In order to tailor MMMs for specific applications, a fundamental understanding of the transport processes in those composites is needed. Without the ability to attribute experimental observations to distinct structural properties of MMMs, technological progress and knowledge acquisition may only rely on empirical approaches. The present work aims in promoting the understanding of the cooperative diffusive processes in MMMs with different morphological properties. Based on gas permeabilities obtainable from permeation experiments with the pure component materials, the presented KMC approach enables prediction of the effective permeation and separation behavior of MMMs of arbitrary mixed-matrix morphologies.

The main focus in this work is put on membranes considered for potential applications in molecular separation. Thus, the effective permeabilities of model mixed-matrix morphologies featuring nonoverlapping ellipsoidal filler particles of different aspect ratios and sizes placed
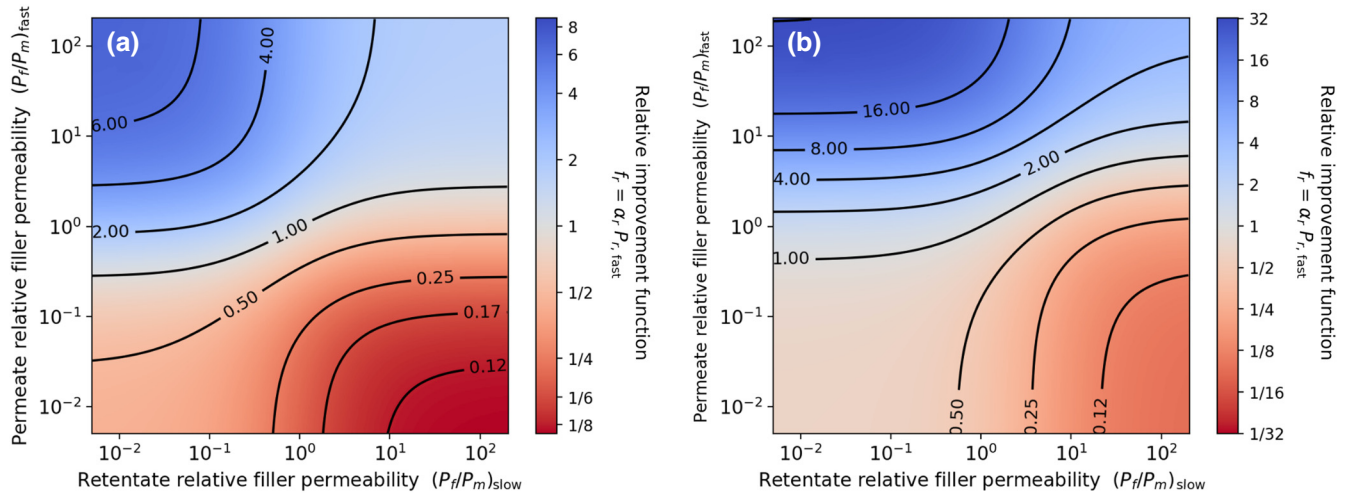
FIG. 12.   Colormaps showing the membrane improvement factor $f_r = \alpha_r P_{r,\text{fast}}$ between fast and slow species for a wide range of relative filler permeabilities for the mixed-matrix compositions with randomly placed disk-shaped (a) and rodlike (b) filler particles featured in Fig. 8 ($\phi = 0.32$). Blue regions are favorable as they indicate an increase in membrane performance due to the filler particles, while red regions exhibit a performance decrease.

randomly or in regular lattice arrangements are extensively presented in the previous section. As a limiting case, the parallel connection of plates models bicontinuous zeolite polymer composite membranes studied in Ref. [34]. Particulate filler distributions with modifications in aspect ratio are studied, for instance, in Ref. [16]. Notably, the presented Monte Carlo approach can easily be extended to study MMMs in which the filler particles
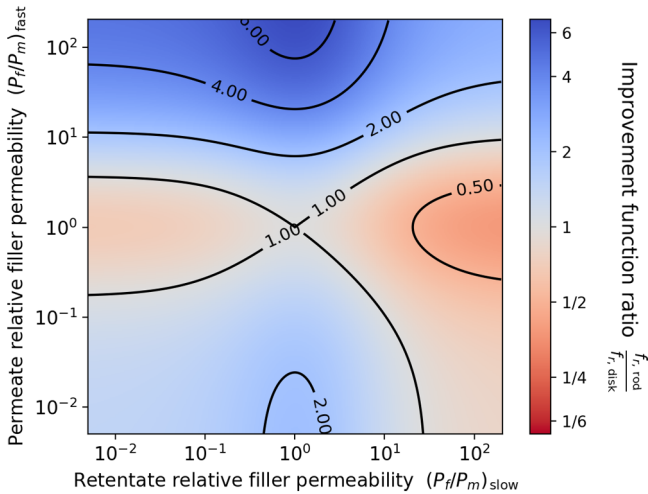

FIG. 13.   Colormap obtained by setting the membrane improvement factors $f_r = \alpha_r P_{r,\text{fast}}$ of the mixed-matrix compositions featuring rodlike and disk-shaped filler particles in relation to each other ($f_{r,\text{rod}}/f_{r,\text{disk}}$). The blue regions in the (fast, slow)-species-relative filler permeability space indicate higher membrane performance for the rodlike over the disk-shaped particles. In the red regions, the disk-shaped particles show superior performance.

may be in contact with each other. Thus, in Ref. [32] the combined experimental and computational study of membranes obtained by pressing the filler particles and filling the remaining space between them with polymer is presented.

In the present work, high compatibility between the polymer matrix and the filler particles is assumed. In other words, the MMMs studied are of ideal morphology as presented in Ref. [24], i.e., possess neither interfacial transport resistances due to pore blockages or rigidified polymer layers nor interfacial voids. Although such nonidealities can easily be incorporated into the present model, in this work we aim at understanding the transport behavior for compatible MMMs first. This knowledge about the ideal MMM permeation enables identification of the effects of incompatibility in real membranes. By comparing the results obtained with the presented KMC approach with permeation measurements of real MMM of similar composition, the compatibility and the type and extent of defects in the sample may be inferred.

Existing transport barriers at the interfaces due to polymeric rigidification or filler pore blockages are expected to lead to a measured effective permeability lower than the ideal MMM permeability. Depending on the mixed-matrix morphology and the permeabilities in the two components these interfacial transport limitations may be marginal to predominant. Surface barriers are especially detrimental in the transport enhancement case, $\mathcal{P}_+$, where they counter the desired effect of amplifying permeation by the filler particles. A related interesting result of our studies is that for relatively low packing fractions the effective permeability of ideal MMMs is independent of the filler-particle size. This is also predicted by

the Maxwell model. Permeation measurements, however, quite commonly exhibit correlations between permeability and particle size at constant volume fraction. This is strong evidence for interfacial defects in the MMMs, since filler-particle size correlates with interface area. In particular, in the case of strong transport limitations at the interfaces, the effective permeability of the MMM declines with shrinking particle size.

On the other hand, measured permeabilities higher than the ideal MMM permeability are a strong indicator for interfacial voids. Similar to the surface barriers' case, the significance of those effects depend on the mixed-matrix morphology and the polymer and filler permeabilities. Void spaces especially impair applications, where transport inhibition by the filler particles is desired ($\mathcal{P}_-$), since they provide the gas molecules with extremely fast pathways around the obstacles. Returning to the particle-size example, with interfacial voids the permeability of the MMM is expected to increase with declining particle size.

V. CONCLUSIONS

As the main finding, correlations between the phase composition and the mass transport in ideal MMMs are established. For this purpose, three-dimensional models of various compositions of polymer and filler subspaces commonly found in real MMMs are created. A kinetic Monte Carlo approach on a discrete lattice gas is employed to emulate the permeation of gas molecules through these mixed-matrix models. By evaluating the effective permeability, the effects of the morphology of the two phases on mass transport is studied in a broad filler permeability range including both transport-inhibition and transport-enhancement scenarios. The limiting cases of planar filler subspaces parallel and perpendicular to the concentration gradient demonstrated the feasibility of the KMC approach. For the considered particulate compositions featuring different filler-particle packing fractions, particle sizes, random versus regular placement, and various particle shapes (aspect ratios), the simulation results for the effective mixed-matrix membrane permeability are in good agreement with theoretical predictions from the literature, such as the Maxwell and Lewis-Nielsen model.

In the range of filler-particle sizes and packing fractions of randomly placed spherical particles studied, the particle size is found to have no significant impact on the permeation behavior. Additionally, changing from the random placement to a regular lattice filler-particle arrangement only slightly modulated the effective membrane permeability and only for high filler permeabilities, showing only small influence of percolation effects for morphologies with nonoverlapping spherical filler particles. These findings supported the analytical models, proving them to be valid for filler particles of different sizes up to packing volume fractions of at least 0.3. However, a significant

influence on mass transport is found upon variation of the filler-particle aspect ratio. Membrane geometries featuring filler particles aligned with their largest principal axis perpendicular to the membrane plane always resulted in higher permeabilities than their counterparts with spherical particles or particles aligned parallel to the membrane plane. The latter configuration is instead more effective in suppressing permeation. Finally, the effect of the particle aspect ratio on the membrane selectivity and performance is evaluated. For the separation of two arbitrarily chosen gas species, predictions are made of which orientation of the filler particles is more favorable for the performance of the MMM.

Generally, the approach presented is able to predict effective permeabilities and selectivities of gases in arbitrary ideal mixed-matrix compositions. This gives deeper insight into the transport behavior in two-phase mixed-matrix membranes and may aid as a guide for choosing effective polymer-filler compositions for applications in gas separation. By comparison of data from permeation measurements, information about the compatibility and the effects of nonidealities arising from the fabrication of the mixed-matrix membrane can be obtained. Additionally, to promote the theoretical understanding of the influence of these nonidealities on mass transport, nonideal mixed-matrix morphologies can readily be modeled with the approach. This may be addressed in future work.

APPENDIX A: VALIDATION OF THE COMPUTATIONAL MODEL

In order to verify the kinetic Monte Carlo approach used in this work, a comparison to numerical calculations of Fick's diffusion performed by Ref. [30] and the analytical models presented in Sec. II A is conducted (see Fig. 14). The mixed-matrix morphology utilized resembles the one used in Ref. [30] (randomly placed nonoverlapping spherical filler particles with a radius of 1/15 of the membrane thickness embedded in the polymer-host membrane). The parameters used are listed in Table 1 of Ref. [30]. For this work, two different approaches are employed to calculate the effective permeabilities of these MMM models, the first by evaluating the steady-state flux of molecules through the membrane (permeation simulations) as described in Sec. II B. In the second approach, the membrane is brought into equilibrium under thermodynamic conditions similar to the conditions of the feed side from the permeation simulations. Then the average equilibrium solubility in the
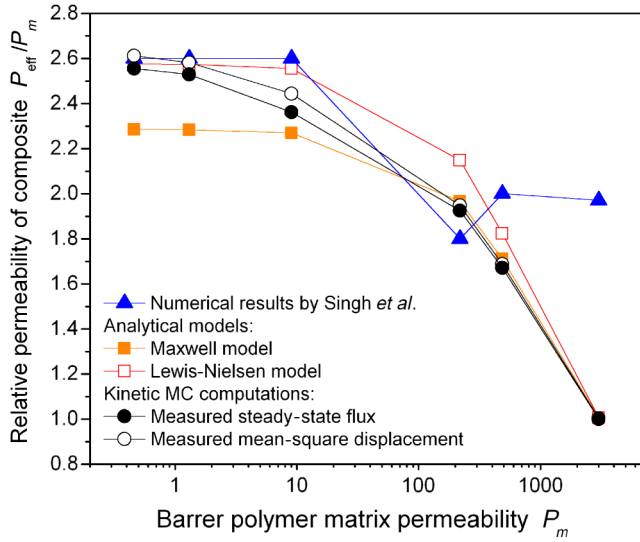
FIG. 14. Relative permeability as a function of the polymer-matrix permeability of MMMs with the polymer-host materials (*from the left- to right-hand side*) Torlon, Ultrem, Matrimid, 6FDA-DAM: DABA 4:1, FDA-DAM, and PDMS, each containing ZIF-8 filler particles. The figure resembles Fig. 9 of Ref. [30]. The *blue triangles* represent the results of Singh *et al.* obtained by finite-element numerical solving of the diffusion equation. The *filled* and *empty squares* indicate the Maxwell and Lewis-Nielsen model, respectively. The *black circles* represent the results obtained with the kinetic Monte Carlo model presented in this work, either by evaluating the steady-state flux through the membrane (*filled*) or by evaluating the concentration and mean-square displacement under equilibrium conditions (*empty*). All permeabilities are obtained considering a filler packing fraction of $\phi = 0.3$.

TABLE I. Parameters used for the fitting curves in Fig. 16(b). The filler packing fraction ϕ is taken from the three-dimensional model geometries.

Shape	ϕ	$\lambda_\parallel$
Disk	0.3228 (fixed)	0.5787 ± 0.0085
Sphere	0.3180 (fixed)	0.7900 ± 0.0058
Rods	0.3216 (fixed)	0.9150 ± 0.0025

MMM, $S_{\text{eff}} \propto c_{\text{eff}}$, and the microscopic diffusion coefficient $D_{\text{eff}} = \langle r^2 \rangle / (6t)$ are evaluated via the mean-square displacement $\langle r^2 \rangle$ of the gas molecules. From here, the relative effective permeability of the MMM can be obtained with Eq. (7) by comparing with the results obtained for the pure polymer-host membrane. The comparison shows that the results of the kinetic Monte Carlo approach resemble the Maxwell model except in the region of large relative filler permeabilities P_f/P_m, where the model is known to be inaccurate. However, in this region, the computational results approach the Lewis-Nielsen model. The permeabilities provided by Ref. [30] can not be explained reasonably, since one would expect different approaches to solve the same equations to yield similar results.

APPENDIX B: REDUCTION OF DIFFUSIVITY AND SOLUBILITY INTO ONE PERMEABILITY PARAMETER

As a proof of principle for the combination of the diffusivity D_k and the concentration c_k of subspace $k \in \{m, f\}$ (membrane, filler) into one permeability parameter
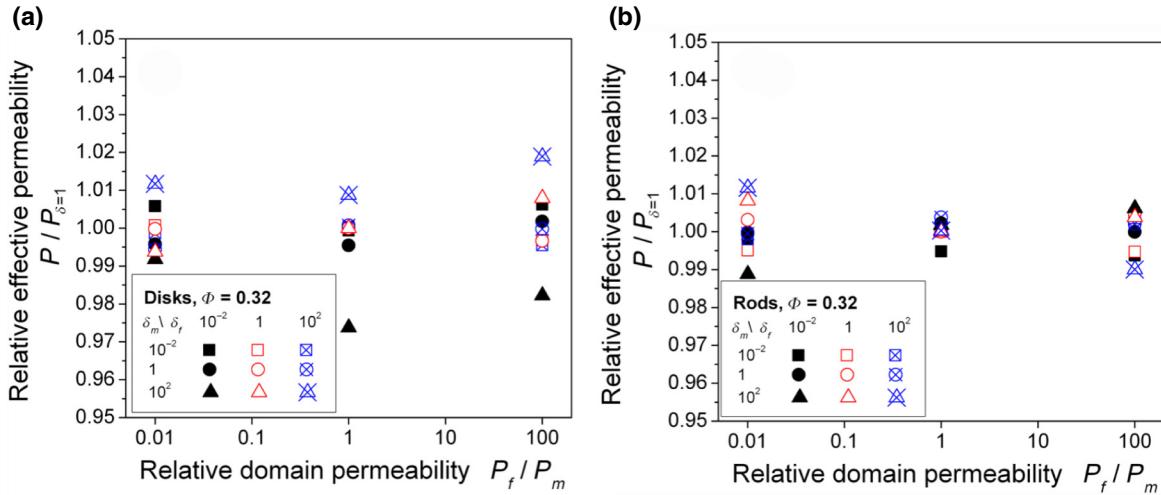

FIG. 15. Deviations in the effective permeability of the MMM with varying D_k and c_k upon constant $P_k \propto D_k c_k$ versus filler permeability relative to the permeability of the pure polymer, P_m. (a) Results for the mixed-matrix composition featuring randomly distributed disks, while the results for (b) are obtained by using the geometry with randomly distributed rodlike filler particles (see Fig. 8). For each relative filler-permeability value indicated by the x axis, the graph features nine different combinations of $\delta_m = D_m/c_m$ and $\delta_f = D_f/c_f$.

$P_k \propto D_k c_k$, simulations are carried out, considering variation of D_k and c_k while keeping P_k and all other conditions constant. These simulations are employed for two mixed-matrix compositions and different relative filler permeabilities (Fig. 15). It can be seen that the largest discrepancy between the results of two different $\{\delta_f, \delta_m\}$ combinations, where $\delta = D/c$, is only approximately 5%, in most of the cases even below 1%. This validates the simplification that the permeability can be used as the only necessary material property for a reasonably accurate description of relative gas transport in each subspace.

APPENDIX C: SIMPLE MODEL CONSIDERING THE FILLER-PARTICLE SHAPE

To predict the effective permeability of membranes with mixed-matrix compositions between the two extreme cases presented in Sec. III A, some simple considerations can be made. Using the simplified structure of a single cuboid filler particle and the symbols presented in Fig. 16(a), Eq. (13) can be rewritten to

$$\frac{P_{\text{eff}}}{P_m} = \lambda_\perp^2 \frac{P'}{P_m} + 1 - \lambda_\perp^2, \tag{C1}$$

where P' can be obtained from Eq. (15):

$$\frac{P_m}{P'} = \lambda_\| \frac{P_m}{P_f} + 1 - \lambda_\|. \tag{C2}$$

Inserting Eq. (C2) into Eq. (C1) and taking into account that $\phi = \lambda_\| \lambda_\perp^2$ yields

$$\frac{P_{\text{eff}}}{P_m} = 1 - \frac{\phi \left(1 - P_f/P_m\right)}{\lambda_\| \left(1 - P_f/P_m\right) + P_f/P_m}. \tag{C3}$$
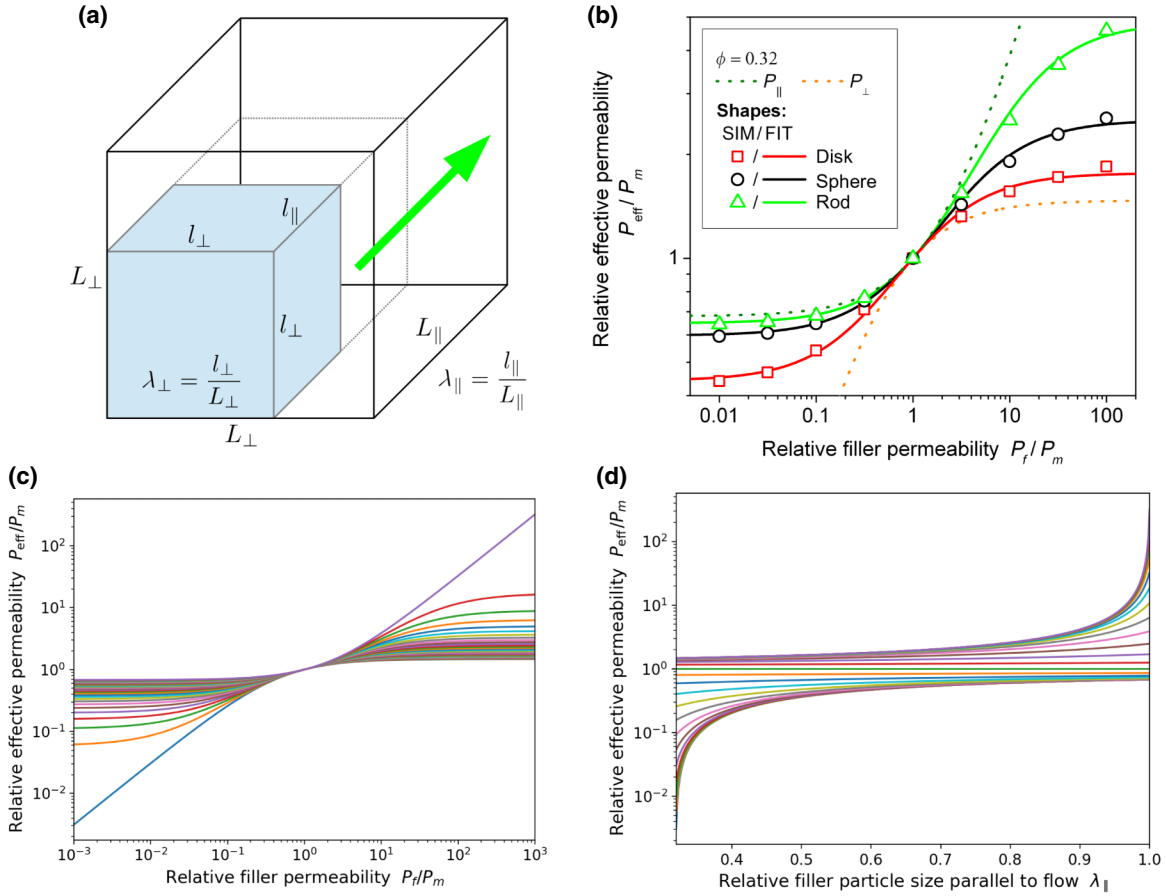

FIG. 16. Model considering the filler-particle size $\|_{\text{flow}}$. (a) Simplified geometry of a mixed-matrix composition with a cuboid filler particle in blue. The direction $\|_{\text{flow}}$ is indicated with the green arrow. The mathematical symbols describe the dimensions of the membrane and the filler particle. (b) Duplicate of Fig. 9(a) showing the effective permeability of mixed-matrix membranes featuring different filler-particle shapes, but with additional fitting curves obtained with Eq. (C3). The corresponding fitting parameters are shown in Table I. (c) Relative effective permeability versus relative filler permeability for different values of $\lambda_\|$ from $\lambda_\| = \phi$ (bottommost curve, resembling the case of plates $\perp_{\text{flow}}$) to $\lambda_\| = 1$ (topmost curve, resembling the case of plates $\|_{\text{flow}}$) obtained from Eq. (C3) for $\phi = 0.32$. (d) Relative effective permeability versus $\lambda_\|$ for different relative filler permeabilities in the range from 10^{-3} (bottommost curve) to 10^3 (topmost curve) as of Eq. (C3) for $\phi = 0.32$. The left end of the x axis represents the case of plates $\perp_{\text{flow}}$, while the right end indicates the case of plates aligned $\|_{\text{flow}}$.

By interpreting $\lambda_\parallel$ more generally as an average measure related to the relative length of continuous filler-particle domains $\parallel_{\text{flow}}$, the above equation can be used to heuristically describe the permeability of more complicated mixed-matrix compositions. This is shown in Fig. 16(b), where Eq. (C3) is used to fit the permeability data obtained from the KMC simulations for the three different shapes of Fig. 8. The fitting parameters are listed in Table I.

Since the filler packing fraction ϕ is known from the mixed-matrix geometries, $\lambda_\parallel$ is the only parameter to be adjusted. It can be seen that the computational results can be approximated quite well with the help of Eq. (C3). This enables the dependency of the effective permeability of the MMM on the filler-particle-size measure $\lambda_\parallel$ to be looked at in more detail, which is done for $\phi = 0.32$ in Figs. 16(c) and 16(d).

[1] J. T. Kiehl and K. E. Trenberth, Earth's annual global mean energy budget, Bull. Am. Meteorol. Soc. **78**, 197 (1997).

[2] A. L. Kohl and R. B. Nielsen, *Gas Purification* (Gulf Publishing, Houston, 1997).

[3] P. Bernardo, E. Drioli, and G. Golemme, Membrane gas separation: A review/state of the art, Ind. Eng. Chem. Res. **48**, 4638 (2009).

[4] M. A. Aroon, A. F. Ismail, T. Matsuura, and M. M. Montazer-Rahmati, Performance studies of mixed matrix membranes for gas separation: A review, Sep. Purif. Technol. **75**, 229 (2010).

[5] L. M. Robeson, Polymer membranes for gas separation, Curr. Opin. Solid State Mater. Sci. **4**, 549 (1999).

[6] L. M. Robeson, The upper bound revisited, J. Memb. Sci. **320**, 390 (2008).

[7] A. Ismail and L. David, A review on the latest development of carbon membranes for gas separation, J. Memb. Sci. **193**, 1 (2001).

[8] J. Caro and M. Noack, Zeolite membranes—recent developments and progress, Microporous Mesoporous Mater. **115**, 215 (2008).

[9] J. Gascon, F. Kapteijn, B. Zornoza, V. Sebastián, C. Casado, and J. Coronas, Practical approach to zeolitic membranes and coatings: State of the art, opportunities, barriers, and future perspectives, Chem. Mater. **24**, 2829 (2012).

[10] R. Mahajan, R. Burns, M. Schaeffer, and W. J. Koros, Challenges in forming successful mixed matrix membranes with rigid polymeric materials, J. Appl. Polym. Sci. **86**, 881 (2002).

[11] R. Mahajan, D. Vu, and W. J. Koros, Mixed matrix membrane materials: An answer to the challenges faced by membrane based gas separations today?, J. Chin. Inst. Chem. Eng. **33**, 77 (2002).

[12] S. Kitagawa, R. Kitaura, and S.-I. Noro, Functional porous coordination polymers, Angew. Chem. Int. Ed. **43**, 2334 (2004).

[13] R. Adams, C. Carson, J. Ward, R. Tannenbaum, and W. Koros, Metal organic framework mixed matrix membranes for gas separations, Microporous Mesoporous Mater. **131**, 13 (2010).

[14] W. J. Koros and C. Zhang, Materials for next-generation molecularly selective synthetic membranes, Nat. Mater. **16**, 289 (2017).

[15] B. Seoane, J. Coronas, I. Gascon, M. Etxeberria-Benavides, O. Karvan, J. Caro, F. Kapteijn, and J. Gascon, Metal-organic framework based mixed matrix membranes: A solution for highly efficient CO_2 capture?, Chem. Soc. Rev. **44**, 2421 (2015).

[16] A. Sabetghadam, B. Seoane, D. Keskin, N. Duim, T. Rodenas, S. Shahid, S. Sorribas, C. Le Guillouzer, G. Clet, C. Tellez, M. Daturi, J. Coronas, F. Kapteijn, and J. Gascon, Metal organic framework crystals in mixed-matrix membranes: Impact of the filler morphology on the gas separation performance, Adv. Funct. Mater. **26**, 3154 (2016).

[17] T. Rodenas, I. Luz, G. Prieto, B. Seoane, H. Miro, A. Corma, F. Kapteijn, F. X. Llabrés I Xamena, and J. Gascon, Metal-organic framework nanosheets in polymer composite materials for gas separation, Nat. Mater. **14**, 48 (2014).

[18] J. C. Maxwell, *A Treatise on Electricity and Magnetism* (Dover Publications, New York, 1954).

[19] R. M. Barrer, in *Diffusion in Polymers*, edited by J. Crank and G. S. Park (Academic Press, London & New York, 1968).

[20] T. B. Lewis and L. E. Nielsen, Dynamic mechanical properties of particulate-filled composites, J. Appl. Polym. Sci. **14**, 1449 (1970).

[21] L. E. Nielsen, Thermal conductivity of particulate-filled polymers, J. Appl. Polym. Sci. **17**, 3819 (1973).

[22] K. G. Papadokostaki, M. Minelli, F. Doghieri, and J. H. Petropoulos, A fundamental study of the extent of meaningful application of maxwells and wieners equations to the permeability of binary composite materials. Part II: A useful explicit analytical approach, Chem. Eng. Sci. **131**, 353 (2015).

[23] J. H. Petropoulos, K. G. Papadokostaki, F. Doghieri, and M. Minelli, A fundamental study of the extent of meaningful application of maxwells and wieners equations to the permeability of binary composite materials. Part III: Extension of the binary cubes model to 3-phase media, Chem. Eng. Sci. **131**, 360 (2015).

[24] H. Vinh-Thang and S. Kaliaguine, Predictive models for mixed-matrix membrane performance: A review, Chem. Rev. **113**, 4980 (2013).

[25] K. A. Fichthorn and W. H. Weinberg, Theoretical foundations of dynamic Monte-Carlo simulations, J. Chem. Phys. **95**, 1090 (1991).

[26] F. J. Keil, R. Krishna, and M. O. Coppens, Modeling of diffusion in zeolites, Rev. Chem. Eng. **16**, 71 (2000).

[27] K. Malek and M. O. Coppens, Pore roughness effects on self- and transport diffusion in nanoporous materials, Colloid Surf. A-Physicochem. Eng. Asp. **206**, 335 (2002).

[28] D. Schneider, D. Mehlhorn, P. Zeigermann, J. Kärger, and R. Valiullin, Transport properties of hierarchical micro-mesoporousmaterials, Chem. Soc. Rev. **45**, 3439 (2016).

[29] E. Marand and A. Surapathi, The role of solubility partition coefficient at the mixed matrix interface in the performance of mixed matrix membranes, J. Memb. Sci. **415-416**, 871 (2012).

[30] T. Singh, D.-Y. Kang, and S. Nair, Rigorous calculations of permeation in mixed-matrix membranes: Evaluation of

interfacial equilibrium effects and permeability-based models, J. Memb. Sci. **448**, 160 (2013).

[31] H. Müller-Krumbhaar and K. Binder, Dynamic properties of the monte carlo method in statistical mechanics, J. Stat. Phys. **8**, 1 (1973).

[32] S. Friebe, A. Mundstock, D. Schneider, and J. Caro, An untrodden path: Versatile fabrication of self-supporting polymer-stabilized percolation membranes (PSPMs) for gas separation, Chem. - A Eur. J. **23**, 6522 (2017).

[33] P. Zeigermann, S. Naumov, S. Mascotto, J. Kärger, B. M. Smarsly, and R. Valiullin, Diffusion in hierarchical mesoporous materials: Applicability and generalization of the fast-exchange diffusion model, Langmuir **28**, 3621 (2012).

[34] I. Kiesow, D. Marczewski, L. Reinhardt, M. Mühlmann, M. Possiwan, and W. A. Goedel, Bicontinuous zeolite polymer composite membranes prepared via float casting, J. Am. Chem. Soc. **135**, 4380 (2013).